Supplementary Information

Flexural strike-slip basins

Derek Neuharth[1,2], Sascha Brune[1,2], Anne Glerum[1], Chris K. Morley[3], Xiaoping Yuan[1,4], Jean Braun[1,2]

[1]GFZ German Research Centre for Geosciences, Telegrafenberg, 14473 Potsdam, Germany.

[2]Institute of Geosciences, University of Potsdam, Germany.

[3]PTTEP, Enco, Vibhavadi-Rangsit Road, Chatuchak, Bangkok, 10900, Thailand

[4]School of Earth Sciences, China University of Geosciences, Wuhan, China

Contents of this file

Additional supporting information (uploaded separately)

Text S1: ASPECT Methods

1.1 Governing equations

We perform numerical simulations of a 3D strike-slip system using the open source finite-element code ASPECT (Advanced Solver for Problems in Earth's ConvecTion, version 2.3.0-pre, commit 886749d; Heister et al., 2017; Kronbichler et al., 2012; Rose et al., 2017; Bangerth et al., 2019). ASPECT solves the following incompressible conservation equations assuming an infinite Prandtl number (i.e., without the inertial term),

$$-\nabla \cdot (2\eta\dot{\varepsilon}) + \nabla P = \rho \mathbf{g}\,, \tag{1}$$

$$\nabla \cdot (\mathbf{u}) = 0\,, \tag{2}$$

$$\bar{\rho} C_p \left(\frac{\partial T}{\partial t} + \mathbf{u} \cdot \nabla T\right) - \nabla \cdot k\nabla T = \bar{\rho} H + \alpha T (\mathbf{u} \cdot \nabla P)\,, \tag{3}$$

$$\frac{\partial c_i}{\partial t} + \mathbf{u} \cdot \nabla c_i = q_i\,, \tag{4}$$

where equation (1) represents the conservation of momentum, with η the effective viscosity, $\dot{\varepsilon}$ the deviator of the strain rate tensor (defined as $\frac{1}{2}(\nabla\mathbf{u} + (\nabla\mathbf{u})^T)$), $\mathbf{u}$ the velocity, P the pressure, ρ the density, and $\mathbf{g}$ gravity. Equation (2) describes the conservation of volume. Equation (3) represents the conservation of energy where $\bar{\rho}$ is the reference adiabatic density, C_p the specific heat capacity, T the temperature, k the thermal conductivity, H the radiogenic heating, and α the thermal expansivity. As right-hand-side heating terms, we include radioactive heating and adiabatic heating, in that order. Finally, we solve the advection equation (4) for each compositional field c_i (e.g., upper crust, lower crust, and accumulated plastic strain) with reaction rate q_i nonzero only for the plastic strain field.

1.2 Rheology

We use a visco-plastic rheology (Glerum et al., 2018), which additionally includes plastic weakening based on accumulated plastic strain. In the viscous regime, we use a composite of diffusion and dislocation creep (Karato and Wu, 1993), formulated as:

$$\eta_{eff}^{diff|dis} = \frac{1}{2} A_{diff|dis}^{\frac{-1}{n}} d^{m} \dot{\varepsilon}_{e}^{\frac{1-n}{n}} \exp\left(\frac{\left(E_{diff|dis} + PV_{diff|dis}\right)}{nRT}\right), \quad (5)$$

where A is a scalar prefactor, d the grain size, $\dot{\varepsilon}_e$ the square root of second invariant of the deviatoric strain rate, E the activation energy, P the pressure, V the activation volume, R the gas constant, T the temperature, and n the stress exponent. For diffusion, n = 1 and the equation becomes independent of strain rate. For dislocation creep, the grain size exponent m vanishes, rendering dislocation creep independent of grain size. Values for A, E, V, and n used in our models are composition-dependent and can be found in supplementary Table S1.

In the plastic regime, when viscous stresses exceed the yield stress, we use the Drucker-Prager yield criterion (Davis and Selvadurai, 2002). The effective plastic viscosity is given by

$$\eta_{eff}^{pl} = \frac{\frac{6C\cos\phi}{\sqrt{3}(3-\sin\phi)} + \frac{6P\sin\phi}{\sqrt{3}(3-\sin\phi)}}{2\dot{\varepsilon}_e}, \quad (6)$$

where C is the cohesion and ϕ the internal angle of friction. The accumulation of plastic strain is tracked as a compositional field. This field is used to linearly weaken ϕ from an initial value of 30° to a final value of 7.5° over the accumulated plastic strain interval of 0 to 1. The time-integrated value of the strain reaction rate q_i is approximated as $\dot{\varepsilon}_e \cdot dt$ when plastic yielding occurs (with dt the current timestep size).

Text S2: FastScape Methods

FastScape is a landscape evolution code that changes the topographic surface through uplift, advection, the stream-power law, and hillslope diffusion (Braun and Willett, 2013). It can additionally deposit fluvial sediment (Yuan et al., 2019a) and include a marine component, which handles marine sediment (sand/silt) transport and deposition, and layer compaction based on sand/silt porosity (Yuan et al., 2019b). It uses a 2D horizontal mesh with a uniform resolution. For simplicity, we here assume that the entire model surface is submarine, with uniform properties (i.e., sand and silt transport coefficients are the same), and that there is no compaction (porosity is zero). Hence, FastScape deforms the surface through the uplift rate and marine diffusion equation only as

$$\frac{\mathrm{dh}}{\mathrm{dt}} = \mathbf{U} + \mathrm{K_m}\nabla^2\mathrm{h}\,, \tag{7}$$

where h is the topographic elevation, $\mathbf{U}$ the uplift rate and $\mathrm{K_m}$ the marine sediment diffusion coefficient.

Text S3: ASPECT/FastScape coupling

In this paper we use a two-way coupling of the tectonic ASPECT code and the landscape evolution FastScape code. For this coupling, a FastScape shared library is called by an ASPECT plugin to deform its surface as described in the previous section. The plugin has three main components: 1) Copy the surface height and velocity values from ASPECT. 2) Initialize and run FastScape at a resolution equivalent to or greater than the one used at the surface of ASPECT. If it is the first timestep of the tectonic model run, FastScape is initialized using height and velocity values from ASPECT. In subsequent timesteps, as FastScape runs separately and can be at a higher resolution than ASPECT, only the velocity values from ASPECT are transferred to FastScape. Before

running FastScape, the initial topography values are saved. After running FastScape, the new and previous topography are compared to determine a nodal vertical (Z) velocity,

$$\mathbf{V_z} = \frac{h_c - h_p}{dt_a}, \tag{8}$$

where h_p is the surface height at the start of the timestep (previous surface), and h_f the surface height after FastScape has been run (current surface), and dt_a the ASPECT timestep. 3) Using the overarching mesh deformation functionality (see Rose et al., 2017), the Z velocity field is interpolated onto the ASPECT surface to determine the displacement of the mesh surface and interior. From there, ASPECT responds to the change in topography calculated by FastScape due to the induced change in forces that is included in the Stokes equations. At the beginning of the next timestep, the updated velocities computed in the previous timestep are sent to FastScape once again.

The FastScape mesh includes an additional element-size layer of ghost nodes compared to the ASPECT surface mesh. The values of surface height on these nodes are not considered when interpolating the surface back to ASPECT and are used primarily to avoid FastScape boundary artifacts being sent to the ASPECT model (e.g., the boundaries do not uplift from advected topography). To avoid possible erroneous sediment flux out or into the model from artificial slopes, each timestep the ghost nodes are updated with the topography and velocity values of the nearest inward node (an ASPECT boundary node).

Besides passing ASPECT's uplift velocities, we use the plugin's FastScape interface to supply additional input to the surface process model in two ways: 1) to add marine background sedimentation via the sediment rain effect, and 2) to add a boundary sediment flux using the ghost nodes. For the sediment rain, at each nodal point we update FastScape with a flat height increase

every ASPECT timestep. Through the diffusion component in equation (7), we prescribe a constant sediment flux at the boundary, assuming that

$$\mathbf{Q} = K_m S , \quad (9)$$

where **Q** is the sediment flux and S the slope. Since K_m and Q are user-set parameters, to achieve this we alter S by uplifting the boundary ghost nodes every ASPECT timestep so that **Q** remains constant.

Text S4: Model setup

In this study we examine how a strike-slip fault responds to sedimentation. We therefore set up a 3D box model with dimensions 100×8×120 km (X, Y, and Z, where Z is the vertical component) and 5 compositions representing a wet quartzite upper crust (Rutter and Brodie, 2004), wet anorthite lower crust (Rybacki et al., 2006), dry olivine lithospheric mantle, wet olivine asthenosphere (Hirth and Kohlstedt, 2003), and a sediment layer that has rheologic parameters identical to wet quartzite, but with density and temperature parameters consistent with sediment (Sippel et al., 2017). The total crustal thickness is set to 8 km (4 km upper crust, 4 km lower crust) based on crustal estimates of the area (7-10 km; Mahattanachai et al., 2021). The lithospheric mantle extends between the Moho and the lithosphere-asthenosphere boundary (LAB) at 40 km depth. The LAB depth, like the crust, has been perturbed by a previous extensional period. The remaining material beneath the LAB is considered asthenosphere (Fig. S1). While there is no initial sediment layer, the top boundary is fixed to a sediment composition so that any top-inflow of material due to topography changes other than uplift is sediment.

The ASPECT model mesh consists of two element sizes: 1 km and 2 km. The upper 8 km of the model is refined at 1 km to best resolve the crust and the forming sediment layer. This high-

resolution area additionally extends to a depth of 35 k from X = 42 km to X = 52 km to better resolve the strike-slip fault. All other areas are kept at 2 km resolution.

The initial temperature above the LAB is determined by a steady-state geotherm (Turcotte and Schubert, 2013), and below by a mantle adiabat. For simplicity, an initial weak zone is seeded through a small perturbation: we raise the LAB locally by 10% of the lithospheric mantle thickness. We fix the top boundary temperature at 0 °C and the bottom boundary at the temperature initially determined from the mantle adiabat at that depth. All other boundaries are set to zero heat-flux.

The coupled model is run for 10 Myr, where the model in the first 5 Myr includes non-zero velocity boundary conditions. During this time, the western boundary is given a strike-slip component of 20 mm/yr (in Y), and an extensional component of 0.2 mm/yr (in X), while the Z-component of velocity is set to no-slip. This gives a total of 100 km of dextral strike-slip motion and 1 km of extension. The small extensional component is introduced to avoid compressional pop-ups that form at the shear zone as the lithosphere subsides due to the sediment load (Fig. S2). The exact extensional value is chosen to accommodate horizontal stress forces related to isostatic compensation. From 5-10 Myr, extension and strike-slip motion stop as the western boundary is set to no-slip in all directions. All other boundary conditions are constant for the entire model run, with the eastern boundary being no-slip in all directions, the north and south boundaries set to periodic to simulate an infinitely long strike-slip fault, the initial lithostatic pressure computed at a reference location prescribed on the bottom boundary to allow for outflow in response to sedimentation, and the top boundary deformed through the use of FastScape.

FastScape is set up with an arbitrarily high sea level so that the entire model is considered submarine. This setup leads to a model with no acting stream power law, and sediment being moved solely through marine sediment diffusion. For simplicity, we additionally assume that there

is no compaction and no difference between sand and silt. As such, we use a diffusion coefficient of 500 m^2/y for both, a value consistent with open marine environments in previous modelling studies (e.g., Rouby et al., 2013). During the syn-strike-slip phase of the tectonic model (0-5 Myr) we supply sediment to the model in two ways: 1) To account for pelagic/hemipelagic sedimentation (sediment rain), we deposit at a constant and uniform sedimentation rate of 0.2 mm/yr. 2) We assume there is an asymmetric off-model source of sediment, similar to the eastern Mergui Ridge for the East Andaman Basin, that inputs sediment into the system from the eastern boundary at a rate of 40 m^2/yr. This is done through equation (9), wherein we uplift the ghost nodes at each timestep so that a constant flux is prescribed through marine diffusion. After this syn-tectonic stage spanning 5 Myr, sediment supply to the system is halted, although marine diffusion continues to work on the topography.

Parameter	Symbol	Units	Sediment	Upper crust	Lower crust	Lithospheric mantle	Asthenosphere
Reference density (at surface conditions)	ρ_0	kg m^{-3}	2520	2700	2850	3280	3300
Thermal expansivity	α	K^{-1}	$3.7 \cdot 10^{-5}$	$2.7 \cdot 10^{-5}$	$2.7 \cdot 10^{-5}$	$3.0 \cdot 10^{-5}$	$3.0 \cdot 10^{-5}$
Thermal diffusivity	κ	$m^2 s^{-1}$	$7.28 \cdot 10^{-7}$	$9.26 \cdot 10^{-7}$	$5.85 \cdot 10^{-7}$	$8.38 \cdot 10^{-7}$	$8.33 \cdot 10^{-7}$
Heat capacity	C_p	J kg^{-1} K^{-1}	1200	1200	1200	1200	1200
Heat production	H	W m^{-3}	$1.2 \cdot 10^{-6}$	$1.5 \cdot 10^{-6}$	$0.2 \cdot 10^{-6}$	0	0
Cohesion	C	Pa	$20 \cdot 10^6$	$20 \cdot 10^6$	$20 \cdot 10^6$	$20 \cdot 10^6$	$20 \cdot 10^6$
Internal friction angle (unweakened)	ϕ	◦	30	30	30	30	30
Strain weakening interval	-	-	[0,1]	[0,1]	[0,1]	[0,1]	[0,1]
Strain weakening factor	ϕ_{wf}	-	0.25	0.25	0.25	0.25	0.25
Creep properties			Sediment	Wet quartzite	Wet anorthite	Dry olivine	Wet olivine
Stress exponent (dis)	n	-	4.0	4.0	3.0	3.5	3.5
Constant prefactor (dis)	A_{dis}	$Pa^{-n} s^{-1}$	$8.57 \cdot 10^{-28}$	$8.57 \cdot 10^{-28}$	$7.13 \cdot 10^{-18}$	$6.52 \cdot 10^{-16}$	$2.12 \cdot 10^{-15}$
Activation energy (dis)	E_{dis}	J mol^{-1}	$223 \cdot 10^3$	$223 \cdot 10^3$	$345 \cdot 10^3$	$530 \cdot 10^3$	$480 \cdot 10^3$
Activation volume (dis)	V_{dis}	m^3 mol^{-1}	0	0	$38 \cdot 10^{-6}$	$18 \cdot 10^{-6}$	$11 \cdot 10^{-6}$
Constant prefactor (diff)	A_{diff}	$Pa^{-1} s^{-1}$	$5.79 \cdot 10^{-19}$	$5.79 \cdot 10^{-19}$	$2.99 \cdot 10^{-25}$	$2.25 \cdot 10^{-9}$	$1.5 \cdot 10^{-9}$
Activation energy (diff)	E_{diff}	J mol^{-1}	$223 \cdot 10^3$	$223 \cdot 10^3$	$159 \cdot 10^3$	$375 \cdot 10^3$	$335 \cdot 10^3$
Activation volume (diff)	V_{diff}	m^3 mol^{-1}	0	0	$38 \cdot 10^{-6}$	$6 \cdot 10^{-6}$	$4 \cdot 10^{-6}$
Grain size (diff)	d	m	0.001	0.001	0.001	0.001	0.001
Grain size exponent (diff)	m	-	2.0	2.0	3.0	0	0

Table S1: ASPECT model parameters. Abbreviations: dis – dislocation creep, diff – diffusion creep.

Parameter	Symbol	Unit	Value
Marine sand transport coefficient	K_{sand}	m^2/yr	500
Surface sand porosity	φ_{sand}	-	0
Sand e-folding depth	z_{sand}	m	0
Marine silt transport coefficient	K_{silt}	m^2/yr	500
Surface silt porosity	φ_{silt}	-	0
Silt e-folding depth	z_{silt}	m	0
Sand-shale ratio	F	-	1
Thickness of transport layer	L	m	100
Sea level	h_{sea}	m	5000

Table S2: FastScape model parameters.

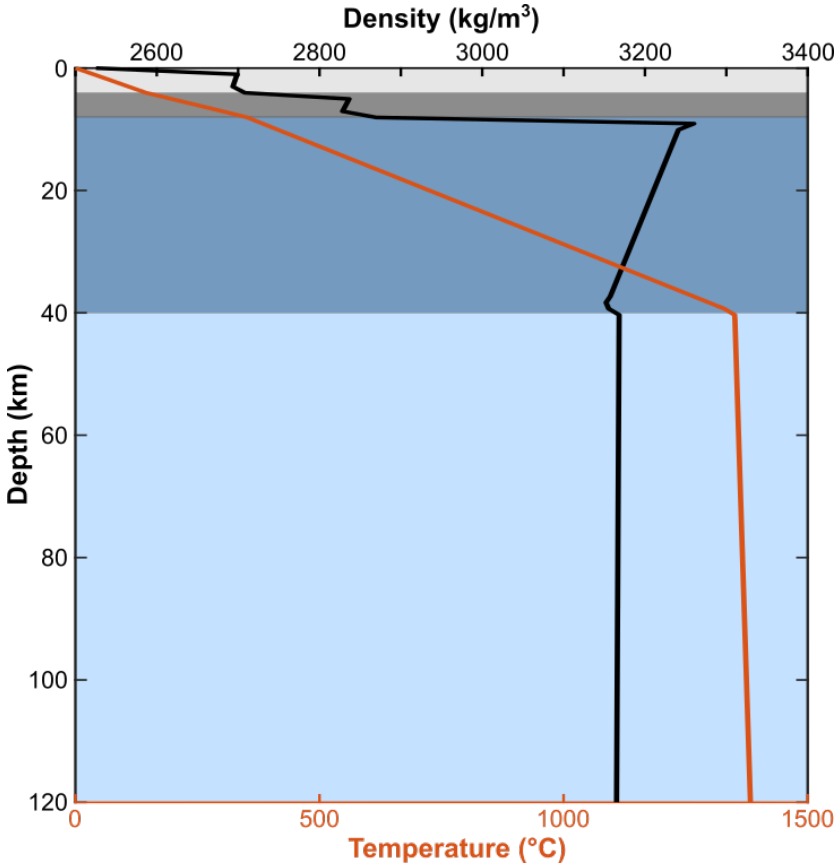

Figure S1: Initial density (black) and temperature (red) profiles with depth. Colored backgrounds represent the initial compositions, with light gray representing the upper crust, dark gray the lower crust, dark blue the mantle lithosphere, and light blue the asthenosphere.

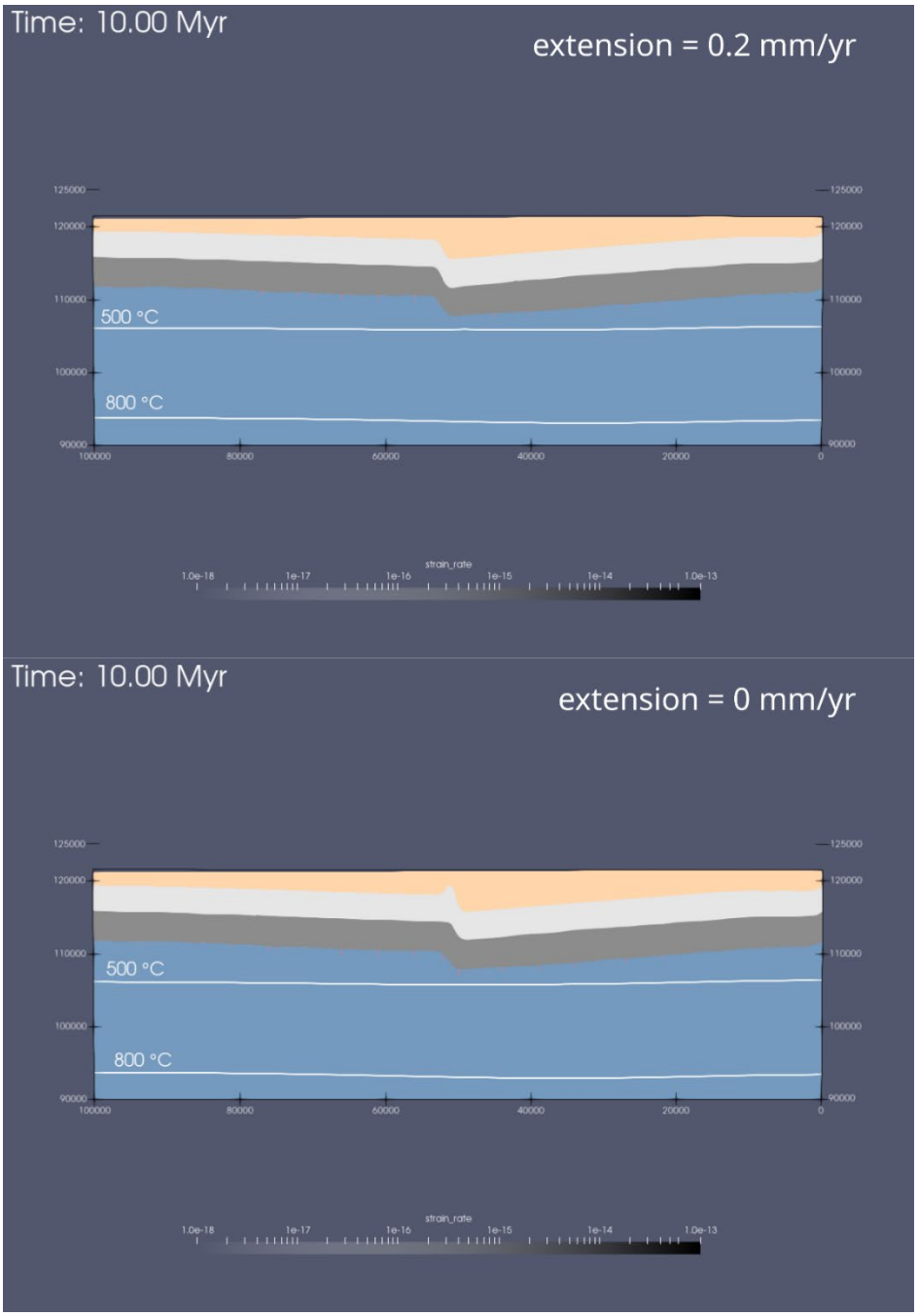

Figure S2: Comparison showing the reference model with A) a 0.2 mm/yr extensional component. B) no extensional component, leading to the formation of a small compressional pop-up in the center.

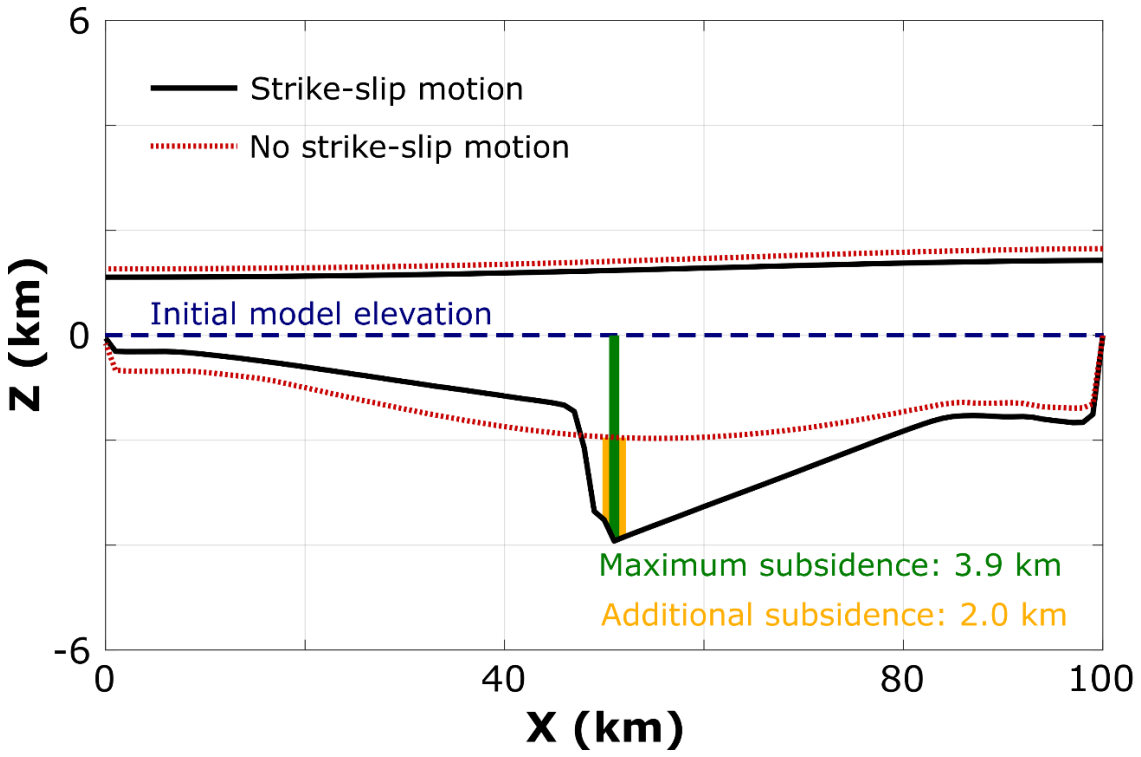

Figure S3: Comparison of the FastScape basement and topography from two models runs: The black curves represent the reference model; the dotted red curves show the reference model without strike-slip motion. The dashed blue line represents the initial model elevation, the green line indicates the total subsidence in the reference model with strike-slip motion, and the yellow line shows the difference in subsidence when comparing models with and without strike-slip motion. In the case without strike-slip motion, maximum subsidence and basin asymmetry are both greatly reduced.

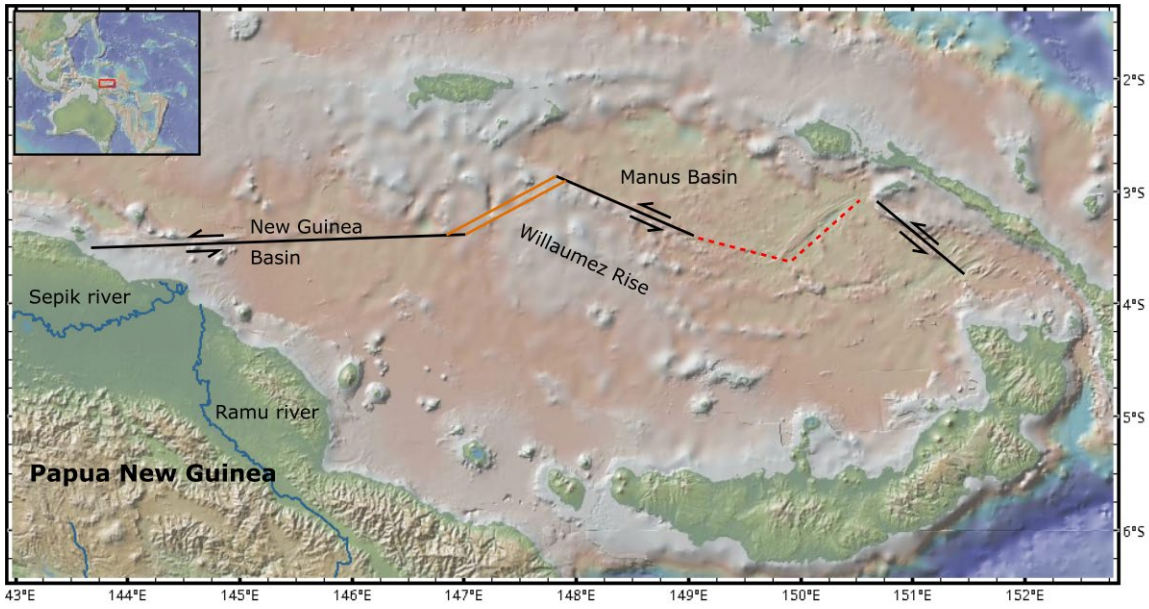

Figure S4: Regional map of the Manus back-arc region, with fault locations based on Fig. 1 in Martinez and Taylor, 1996. Black lines indicate strike-slip faults, parallel orange lines spreading centers, dashed red lines lava fields, and blue lines major rivers. This figure was made using GeoMappApp (www.geomapapp.org; Ryan et al., 2009).

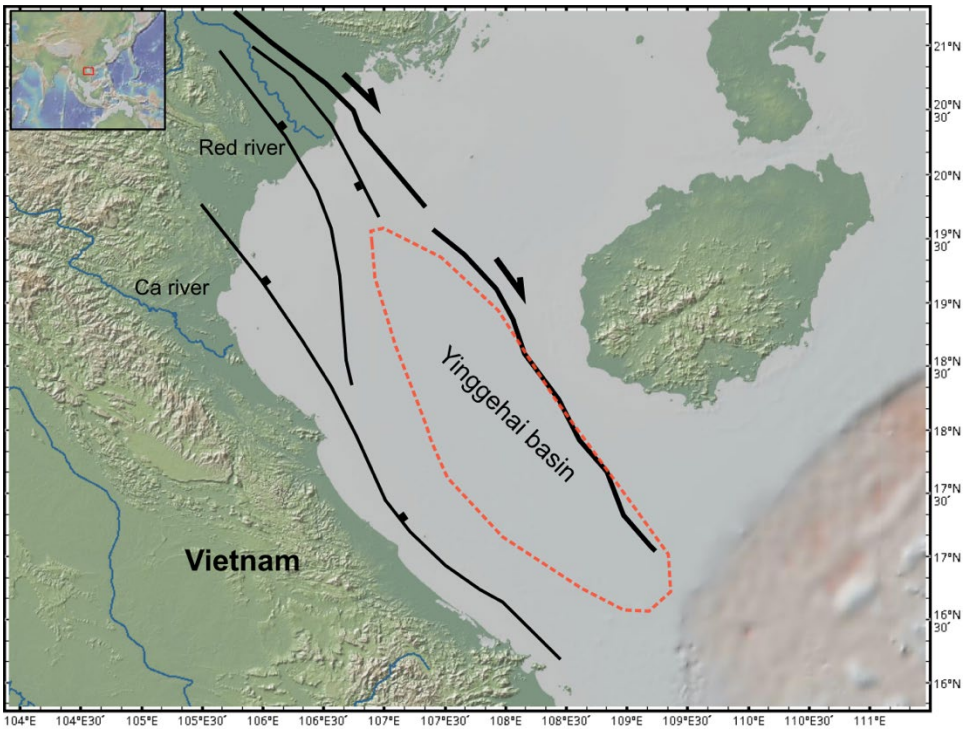

Figure S5: Regional map showing the Red River Fault Zone and location of the Yinggehai basin. Fault locations based on Fig. 10 in Noda, 2013. Black lines show faults, blue lines major rivers, and the Yinggehai basin is outlined in the dashed orange circle. This figure was made using GeoMappApp (www.geomapapp.org; Ryan et al., 2009).

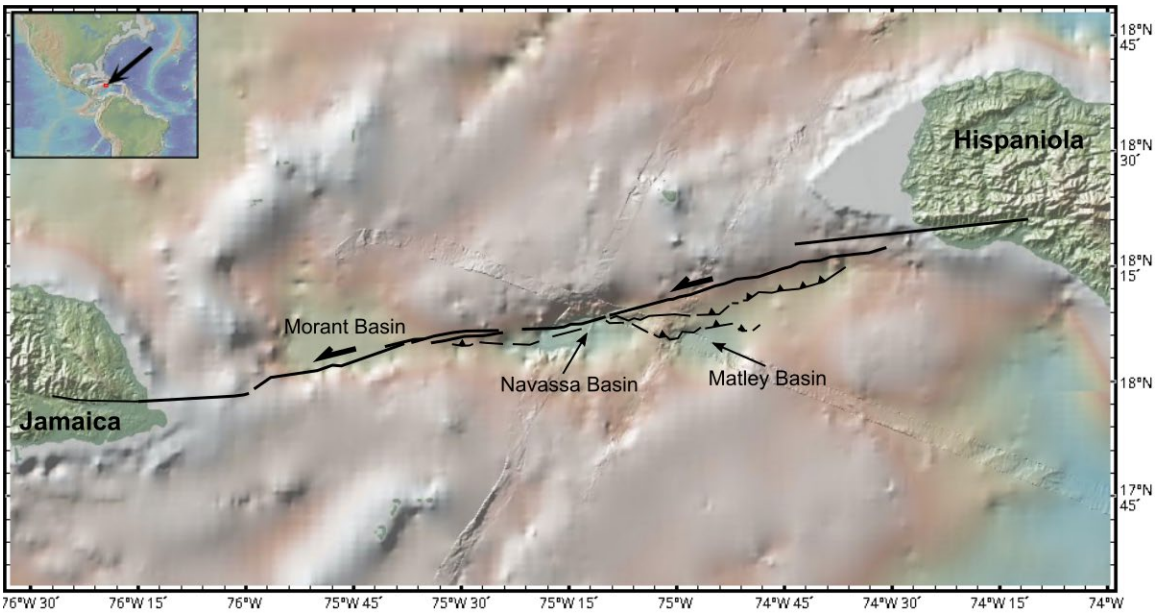

Figure S6: Regional map of the Jamaica Passage showing the Navassa strike-slip basin along the Enriquillo-Plantain-Garden Fault Zone. Fault locations based on Fig. 6 in Corbeau et al., 2016. This figure was made using GeoMappApp (www.geomapapp.org; Ryan et al., 2009).

Video S1: Full evolution of the tectonic reference model (Fig. 2C,K,G). Colors represent composition where tan is sediment, light gray is upper crust, dark gray is lower crust, dark blue is mantle lithosphere, and light blue is the asthenosphere. The white lines are temperature contours, gray-scale the strain rate, and arrows indicate the total velocity magnitude.

Video S2: Evolution of the middle slice of the top 30 km of the reference tectonic model. Colors represent composition where tan is sediment, light gray is upper crust, dark gray is lower crust, dark blue is mantle lithosphere, and light blue is the asthenosphere. The white lines are temperature

contours, gray-scale the strain rate, and red arrows indicate the subsidence rate (Z velocity) along the 8 km depth contour.

References

Bangerth, W., Dannberg, J., Gassmoeller, R., and Heister, T., 2019, ASPECT v2.1.0: Zenodo, https://doi.org/10.5281/zenodo.2653531.

Braun, J., and Willett, S.D., 2013, A very efficient O(n), implicit and parallel method to solve the stream power equation governing fluvial incision and landscape evolution: Geomorphology, v. 180–181, p. 170–179, doi:10.1016/j.geomorph.2012.10.008.

Corbeau, J., Rolandone, F., Leroy, S., Mercier de Lépinay, B., Meyer, B., Ellouz-Zimmermann, N., and Momplaisir, R., 2016, The northern Caribbean plate boundary in the Jamaica Passage: Structure and seismic stratigraphy: Tectonophysics, v. 675, p. 209–226, doi:10.1016/j.tecto.2016.03.022.

Davis, R.O., and Selvadurai, A.P.., 2002, Plasticity and Geomechanics: Cambridge University Press.

Glerum, A., Thieulot, C., Fraters, M., Blom, C., and Spakman, W., 2018, Nonlinear viscoplasticity in ASPECT: Benchmarking and applications to subduction: Solid Earth, v. 9, p. 267–294, doi:10.5194/se-9-267-2018.

Heister, T., Dannberg, J., Gassmöller, R., and Bangerth, W., 2017, High Accuracy Mantle Convection Simulation through Modern Numerical Methods – II: Realistic Models and Problems.: Geophysical Journal International, v. 210, p. 833–851, doi:doi:10.1093/gji/ggx195.

Hirth, G., and Kohlstedt, D., 2003, Rheology of the upper mantle and the mantle wedge: a view from the experimentalists: Inside the Subudction Factory Geophysical Monograph (American Geophysical Union), v. 183.

Karato, S., and Wu, P., 1993, Rheology the Upper Mantle : Synthesis: v. 260.

Kronbichler, M., Heister, T., and Bangerth, W., 2012, High Accuracy Mantle Convection Simulation through Modern Numerical Methods.: Geophysical Journal International, v. 191, doi:doi:10.1111/j.1365-246x.2012.05609.x.

Mahattanachai, T., Morley, C.K., Charusiri, P., and Kanjanapayont, P., 2021, The Andaman Basin Central Fault Zone, Andaman Sea: Characteristics of a major deepwater strike-slip fault system in a polyphase rift: Marine and Petroleum Geology, p. 104997, doi:10.1016/j.marpetgeo.2021.104997.

Martinez, F., and Taylor, B., 1996, Backarc spreading, rifting, and microplate rotation, between transform faults in the Manus Basin: Marine Geophysical Researches, v. 18, p. 203–224, doi:10.1007/BF00286078.

Noda, A., 2013, Strike-Slip Basin – Its Configuration and Sedimentary Facies: Mechanism of

Sedimentary Basin Formation - Multidisciplinary Approach on Active Plate Margins, doi:10.5772/56593.

Rose, I., Buffett, B., and Heister, T., 2017, Stability and Accuracy of Free Surface Time Integration in Viscous Flows.: Physics of the Earth and Planetary Interiors, v. 262, p. 90–100, doi:doi:10.1016/j.pepi.2016.11.007.

Rouby, D., Braun, J., Robin, C., Dauteuil, O., and Deschamps, F., 2013, Long-term stratigraphic evolution of Atlantic-type passive margins: A numerical approach of interactions between surface processes, flexural isostasy and 3D thermal subsidence: Tectonophysics, v. 604, p. 83–103, doi:10.1016/j.tecto.2013.02.003.

Rutter, E.H., and Brodie, K.H., 2004, Experimental grain size-sensitive flow of hot-pressed Brazilian quartz aggregates: Journal of Structural Geology, v. 26, p. 2011–2023, doi:10.1016/j.jsg.2004.04.006.

Ryan, W.B.F. et al., 2009, Global Multi-Resolution Topography synthesis: Geochemistry, Geophysics, Geosystems, v. 10, doi:https://doi.org/10.1029/2008GC002332.

Rybacki, E., Gottschalk, M., Wirth, R., and Dresen, G., 2006, Influence of water fugacity and activation volume on the flow properties of fine-grained anorthite aggregates: Journal of Geophysical Research: Solid Earth, v. 111, doi:10.1029/2005JB003663.

Sippel, J., Meeßen, C., Cacace, M., Mechie, J., Fishwick, S., Heine, C., Scheck-Wenderoth, M., and Strecker, M., 2017, The Kenya rift revisited: Insights into lithospheric strength through data-driven 3-D gravity and thermal modelling: Solid Earth, v. 8, p. 45–81, doi:10.5194/se-8-45-2017.

Turcotte, D.L., and Schubert, G., 2013, Geodynamics: Cambridge University Press.

Yuan, X.P., Braun, J., Guerit, L., Rouby, D., and Cordonnier, G., 2019a, A New Efficient Method to Solve the Stream Power Law Model Taking Into Account Sediment Deposition: Journal of Geophysical Research: Earth Surface, v. 124, p. 1346–1365, doi:10.1029/2018JF004867.

Yuan, X.P., Braun, J., Guerit, L., Simon, B., Bovy, B., Rouby, D., Robin, C., and Jiao, R., 2019b, Linking continental erosion to marine sediment transport and deposition: A new implicit and O(N) method for inverse analysis: Earth and Planetary Science Letters, v. 524, p. 115728, doi:10.1016/j.epsl.2019.115728.